Verification and Performance Optimisation of New RPC Detectors for ATLAS Phase 2

Summer student report

Francesca Scrivano

Advisor: Marco Schioppa, Barbara Liberti, Gregorio Falsetti

September 13, 2024

Contents

1 Upgrade del rivelatore ATLAS: Fase II

The high luminosity upgrade of the LHC (HL-LHC) will allow pp collisions to be achieved with an energy at the centre of mass of $\sqrt{s} = 14$ TeV and a luminosity that can reach $7 \times 10^{34} cm^{-2}\mathrm{s}^{-1}$, accumulating a total integrated luminosity of $3000\mathrm{fb}^{-1}$. Prior to the start of HL-LHC operations, the ATLAS detector will undergo a second and final upgrade, called *Phase II*, planned during *Long Shutdown 3* (LS3) in the period 2024-2026.

One of the main challenges for the muon spectrometer (MS) will be to maintain the ability to identify and track muons, despite the much more demanding working conditions, characterised by higher particle rates, more radiation and a greater number of inelastic pp interactions per bunch crossing.

1.1 The ATLAS Muon Spectrometer

The ATLAS muon spectrometer is a large apparatus with a complex geometry. It is divided into 16 sectors, each associated with one of eight toroidal magnet coils. Four different gas detector technologies are used to cover the entire surface of the barrel and endcap:

- **Monitored Drift Tubes** (MDT) and **Cathode Strip Chambers** (CSC) for precision measurement of coordinates in the plane of curvature.
- **Resistive Plate Chambers** (RPC) and **Thin Gap Chambers** (TGC) for the measurement of the second coordinate and the generation of trigger signals in the barrel and endcap regions.

1.2 Planned Updates in Phase II

The Phase II upgrade of the ATLAS muon spectrometer (MS) involves installing new chambers, replacing some existing chambers and upgrading most of the front-end, trigger and readout electronics. The current electronics are not suitable for handling a level 0 trigger (L0) operating at 1 MHz. To handle coincidences, external programmable FPGAs will be used, replacing the current customised ASICs in the detectors. This change will lead to a more robust, simple and flexible trigger system. In addition, the readout electronics will be upgraded with data multiplexers and high-bandwidth optical links to transmit coincidence information from the detector side to the L0 trigger logic.

The MDT system will have to guarantee high reconstruction efficiency and good pulse resolution, even in the presence of high pile-up and high background rates. Although the HL-LHC imposes more difficult conditions, the system will still have to identify and reconstruct muons accurately. However, muon triggering will require significant upgrades to maintain current pulse thresholds while keeping the trigger rate at manageable levels.

1.3 The New RPC Detectors

A gas detector is a device in which the passage of a charged particle through the gas causes a series of primary ionisations of electrons and ions. The electrons can acquire enough energy on their way to ionise further atoms, triggering an avalanche multiplication. However, it is essential to avoid uncontrolled discharges, which can occur if the detector is subjected to too high an electric field.

The resistive plate chamber detector (RPC) is a type of gas detector. In this system, the gas is sandwiched between two layers of resistive material, usually Bakelite. These layers are connected to a high voltage, creating a high potential difference between the two electrodes, sufficient to trigger an avalanche multiplication within the gas.

The main requirements of the ATLAS RPC system include:

- **Fast tracking** to discriminate the transverse momentum of the muon p_T;
- **High temporal resolution** to accurately identify bunch collision events;

- **High rate handling capability** to deal with the background dominated by neutrons and gamma rays at low p_T;
- **Second-coordinate measurement** with a resolution of 5-10 mm.

To meet these requirements, numerous studies were conducted to design a suitable detector. An ATLAS RPC unit consists of two independent active detector layers, each equipped with two orthogonal strip readout panels, allowing separate measurements of the η and ϕ coordinates.

1.3.1 RPC Structure of Trigger

The new BI RPCs are units equipped with three 1 mm gas gaps and thin 1.4 mm electrodes. They are equipped with frontend electronics on both faces and offer a time resolution of 0.5 ns and a spatial resolution of less than 1 cm. The RPCs are enclosed in a single mechanical case that reinforces the Faraday cage, with an overall thickness of 5 cm.
In my experience, I have used the following trigger RPCs, which I describe below: The first layer of the active detector includes:

- A panel of collection strips segmented in the azimuthal direction (ϕ);
- A flat Bakelite chamber with a 2 mm thick layer of active gas;
- A plastic film insulating the high-voltage side of the bakelite chamber from a second panel of collection strips, segmented along the longitudinal direction (η).

A central support panel, made from a sandwich of honeycomb cardboard and aluminium sheets, acts as an electromagnetic shield, preventing interference between the two detector layers.

The second layer of the active detector is identical to the first, but is mounted in reverse order. A support panel, made of honeycomb board and aluminium sheets, or with aluminium sheets on the outer sides, provides the necessary mechanical robustness.

In addition, a 100 kΩ shunt resistor connects the gas volume to the electromagnetic shielding, allowing measurement of the current flowing in the gas when high voltage (dark current) is applied. The total thickness of an RPC module is about 100 mm, while the active area varies from about 0.4 m for the smallest units to over 1.5 m for the largest ones.

When an ionising particle passes through the gas inside the gap, and an electric field is applied to the electrodes, an avalanche is triggered. The strips pick up an electrical signal, the amplitude of which depends on the distance between the strip and the avalanche. This system of identical strips, oriented on both sides of the gas gap, is able to reconstruct the position of the avalanche in the central plane of the gas gap with a spatial resolution better than 1 cm in both directions η and ϕ.

2 Test Setups for New ATLAS Detectors

We are developing a test set-up to verify the performance of new detectors for the ATLAS experiment. The aim is to ensure that these detectors meet all the necessary requirements, such as *spatial and temporal resolution* and *operational efficiency*.

To realise this setup, we have built a test tower using four detectors identical to those already present in ATLAS. These detectors will be used to generate the trigger and track the cosmic particles through the new detectors to be tested. There are currently four RPC-BO Large (BOL) singlet detectors in the tower, the same as those installed in ATLAS.

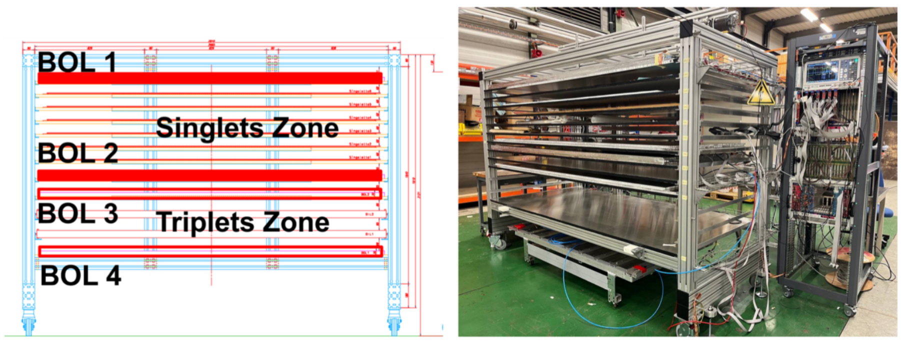

Figure 1: Left: diagram of the structure with the four BOLs highlighted. The singlet test zone at the top and the triplet zone at the bottom. Right: Fully assembled cosmic ray test bench at CERN.

.

The tower is designed to perform trigger and tracking functions on the new detectors, allowing us to verify their performance quickly and efficiently, in a matter of days, even on a large number of devices. The setup will be able to handle a total of six singlet and three triplet detectors to simulate real operating conditions.
In addition, we are working on integrating data from ATLAS's legacy RPC detectors with data from the new, upgraded BI detectors to create a test system that faithfully reflects the conditions of the real experiment. Once the new trigger cards are available, we will be able to fully test the interaction between the existing ATLAS detectors and the new generation detectors. This approach will allow us to validate the overall performance of the system before final implementation.

2.1 Chamber assembly

The test tower taken into consideration as mentioned above consists of four BOLs, in this paragraph I will list the procedure we carried out to build them.

1. **Mechanical cleaning**: Clean the ϕ (phi) and η (eta) panels using a brush, paper and vacuum cleaner to remove any dust and debris.

2. **Frontend Testing**: Perform Frontend testing on the ϕ and η panels, recovering damaged strips where possible.

3. **Panel positioning and alignment** ϕ: Align and position the panel ϕ precisely on the mechanical structure.

4. **Applying copper tape**: Place the copper tape tabs on the *ground* side of the panel ϕ, necessary to seal the sandwich structure.

5. **Positioning the gas gap**: Carefully position and align the *gas gap* on the ϕ panel.

6. **Positioning the PET layer**: Insert the PET layer over the *gas gap*.
7. **Positioning and Alignment of the Panel η**: Carefully align and position the *eta* panel over the PET layer.
8. **Closure of copper tabs**: Glue the copper tabs on the *ground* side of the *eta* panel to complete the closure.
9. **Positioning the last mechanical structure**: Place the last part of the mechanical structure.
10. **Alignment**: With the help of a square, ensure that all parts are perfectly aligned.
11. **Insertion of polystyrene shims**: Insert polystyrene shims between the mechanical structure and the *eta* panel to protect the frontend boards from bending.
12. **Closing the singletons with cloth tape**:
    - a singlet with one layer of 7.5 cm wide cloth tape.
    - another singlet with two overlapping layers of 5 cm wide cloth tape.
13. **Final closure with aluminium tape**: Seal everything with aluminium tape.
14. **Placement in the tower**: The panels were placed in the predefined positions BOL 3 and BOL 4 within the tower.

Figure 2: Cleaning the mechanics

Figure 3: Applying copper tape

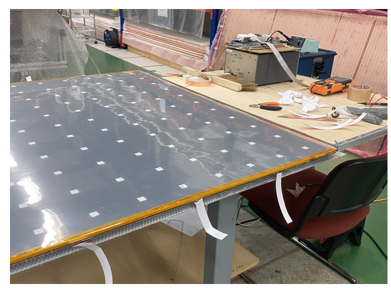

Figure 4: Positioning of the gas gap

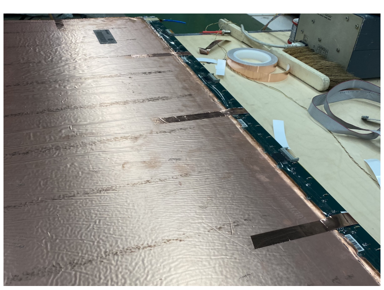

Figure 5: Closure of copper tabs

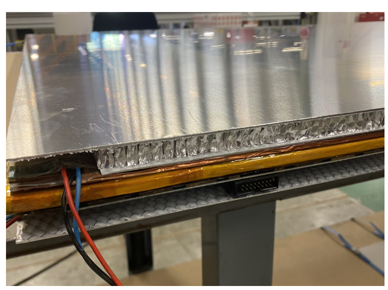

Figure 6: Alignment of BOL layers

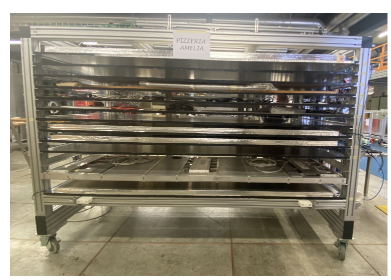

Figure 7: Placement in the tower

Figure 8: Chamber assembly

2.2 HV management

In the context of the data acquisition system, the proper handling of front-end (FE) cards and high voltage modules (up to 12 HV) is crucial. FE cards, which are essential for collecting signals from detectors, have specific power requirements depending on the type of card and their application.
The test tower is powered by a Mainframe CAEN, which handles the high voltage, and a Gossen generator, responsible for the low voltage. The high voltage can be monitored and controlled remotely by accessing the CAEN device via a dedicated interface. During my experience, we also developed a control system programme (DCS) to automate the voltage ramping.

2.3 Gas Management

The gas management system used to supply the tower consists of a power rack, which contains gas control and measurement instruments, such as flow meters and valves, and a series of pipes for gas inflow and outflow. The installation and configuration of the system follows a specific procedure to ensure that the gas mixture flows correctly into the RPC chambers.
The gas enters the power rack through a thinner **blue** tube located at the top of the rack, and exits through a wider **white** tube, also located at the top of the rack.

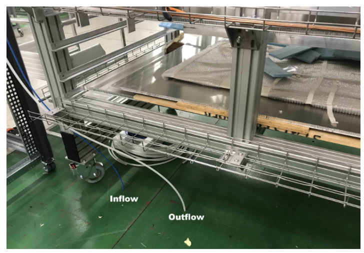

Figure 9: blue tobo: inflow; white tube: outflow

Gas flow from the power rack to the **PC** chamber is via a **blue** tube connected to the rack panel, while the return of gas from the RPC chamber to the power rack is via a **black** tube, also located on the rack panel. To make the gas flow inside the **RPC**, the valves in the gas station must be opened. The gas control system was recently upgraded with the installation of the **FlowSuite** software, which allows all flow parameters to be controlled.

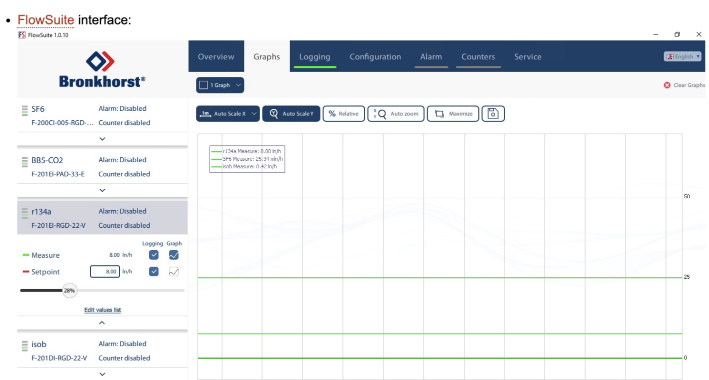

Figure 10: "Flowsuite" interface

The interface shown in the picture belongs to Bronkhorst's **FlowSuite** software, which is used to monitor and control gas flows. Below is a description of the main functionalities that can be managed via this interface:

On the left-hand side of the screen, there are the gases that can be monitored: **SF6**, **CO2**, **r134a**, **isob**), each associated with a specific flowmeter. For each of these flows, it is indicated whether the alarms are enabled or disabled (e.g. 'Alarm: Disabled') and whether the counter is enabled or disabled. In the middle/right part of the screen is a graph representing the measured flows over time. You can see the trend of each gas with a coloured line (green for **r134a**, grey for **SF6**, etc.). The X scale represents time, while the Y represents the gas flow (in l/h).
The gas mixture used in my case is:

- **SF6 (Sulphur Hexafluoride)**: 24.31 ml/h
- **r134a (Tetrafluoroethane)**: 7.67 l/h
- **isob (Isobutane)**: 0.4 l/h

3 The Detector Control System (DCS) and the Trigger and Data Acquisition System (TDAQ)

The Detector Control System (DCS) and the Trigger and Data Acquisition (TDAQ) system are essential to ensure efficient monitoring and data collection of scientific operations.

3.1 DCS system

In collaboration with my supervisors, we developed an advanced voltage ramping programme designed to gradually increase voltages using variable steps. This programme offers an intuitive user interface that simplifies the execution of several crucial operations, including:

- **Opening of the high voltage** (c)
- **Closure of high voltage** (d)
- **Starting the ramping of currents** (e)
- **Start of a new data acquisition** (f)

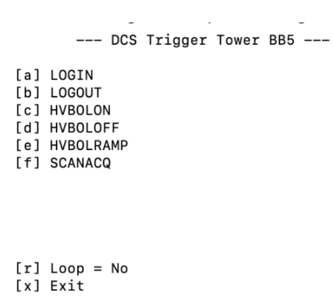

Figure 11: DCS system interface

Our programme differs from the traditional CAEN system for several reasons:

1. **Gradual and Controlled Ramping**: Unlike the CAEN system, which may require manual intervention and offers less precise control, our script handles voltage ramping automatically. The programme uses a list of high voltage (HV) values and gradually ramps up to each specified value. During this process, it verifies that all voltages reach the desired values and checks for abnormal currents. After a short wait to ensure stability, it proceeds to the next value. This function, referred to as (e), improves the efficiency and safety of voltage ramping, reducing the risk of human error.

2. **Data Acquisition Automation**: Function (f) is already fully operational and allows the script `launchacquisition.sh` to be started automatically directly from the programme. This integration makes it possible to perform automatic scans on BIs (Bulk Ionisation), thereby optimising data management and acquisition.

3. **Lack of Trending and Archiving Values**: Although the current system does not yet include trending and archiving of values, a future improvement in this direction is planned. Data archiving and monitoring over time are essential for long-term management and analysis, and will be integrated to provide a more complete picture of system performance.

In summary, our programme offers significant improvements over the CAEN system due to its ability to automate and optimise the ramping of voltages and currents, while the integration of automated data acquisition management is a further advantage. The next step will be the integration of trending and value storage for more complete and detailed control.

3.2 TDAQ system (Trigger and Data acquisition)

3.2.1 Reading chain and uilized electronics

In our data acquisition system, the receiver is responsible for handling the signal coming from the front-end electronics (FE) boards. Each receiver is designed to collect and convert single-output ECL (Emitter-Coupled Logic) signals into NIM (Negative-Input Mode) or TTL (Transistor-Transistor Logic) signals, as required. The receiver performs a logical OR of the signals from the eight channels of each individual FE card, aggregating the signals into a single output. Each receiver column handles eight FE boards. Since we have a total of 56 FE boards (10 phi + 4 eta for each of the 4 BOL chambers), the configuration requires the use of seven receivers. The VME (Versa Module Europa) system comprises a V1718 USB-VME bridge, four V812 discriminators, a V1190A TDC and a V2495 logic unit. The discriminators are configured with a threshold of 150 mV and produce an output signal with a duration of 130 ns.

In this experiment, two types of trigger logic were used: one based on NIM modules and the other using an FPGA.

3.2.2 NIM trigger logic

This signal is sent to the NIM coincidence unit, which coincides the signals from the BOLs. The configuration of the readout chain can vary according to the requirements of the test, and changes must be carefully documented and updated. The TDC (Time-to-Digital Converter), model V1190A, plays a crucial role in the conversion of time signals. It receives output signals from the discriminators in differential ECL format and converts them into digital time data with an acquisition window set to 1.5 microseconds. The signals are transmitted to the TDC via Robinson Nugent cables and acquired via a USB connection to the CAEN V1718 bridge, which is connected to a PC for data recording and analysis. During my experience, I have constructed the TDC channel map, which is an essential document that maps the channels of the TDC for data analysis. This document allows you to configure the data analysis programmes according to your current configuration.

3.2.3 FPGA trigger logic

Each RPC-BOL unit determines the position $P(x, y)$ crossed by a charged particle of a cosmic ray. Trigger events occur when four points are aligned within a time window of a few tens of nanoseconds. On the long side of the chamber there are 10 front-end (FE) boards handling 80 strips, while on the short side there are 4 FE boards handling 24 strips. The output signals from the FE RPC-BOL boards are sent to a TTL receiver and then to a discriminator. The discriminated signal is then sent to a CAEN logic trigger unit, which uses an integrated FPGA to create up to 130 topology trigger configurations. The trigger signal is obtained by combining signals through a logic operation. Within each chamber, a logical AND is performed between the ORs of the 4 strips on the short dimension (coordinates along η) and the ORs of the 10 strips on the long dimension (coordinates along ϕ). The result of this operation is then combined with that of the other chambers using a further logical AND.

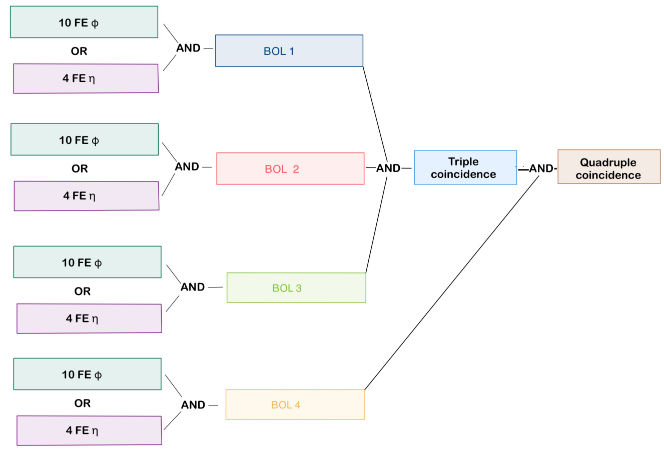

Figure 12: Trigger Logic

FPGA programming

The signal is sent from the discriminator to both the TDC (Time-to-Digital Converter) and the FPGA. I programmed the FPGA using software called 'Sci-Compiler', implementing the trigger logic described above.

To implement this logic, I performed the logical OR operation between the channel pins associated with the eta and phi coordinates. Next, I applied an AND gate between these two coordinates for each individual RPC (Resistive Plate Chamber). This process was repeated for each RPC.

Finally, I implemented a coincidence logic: I used an AND gate between three RPCs to obtain a triple coincidence and another AND gate between four RPCs to obtain a quadruple coincidence. This trigger logic makes it possible to detect significant events by combining the signals from the different RPCs.

4 Tower test

4.1 Scan HV

RPCs (Resistive Plate Chambers) are detectors that exploit charge multiplication through the ionisation process of the gas inside them. The behaviour of the measured current as the applied voltage changes is divided into two distinct phases:

- **Linear (ohmic) behaviour)**: At low voltages, the electric field inside the detector is not strong enough to cause the electrons to multiply. In this regime, the current flowing through the chamber follows Ohm's law:
$$I = \frac{V}{R}$$
dove I is the current, V is the applied voltage and R is the internal resistance of the detector. The gas, at this stage, behaves as an insulator or a weak conductor and no significant charge multiplication is observed.

- **Exponential behaviour (avalanche multiplication)**: Above a certain voltage threshold, the electric field becomes high enough to cause an avalanche multiplication of electrons. The current then begins to grow exponentially as the voltage increases:
$$I(V) \propto e^{\alpha V}$$
where α is a factor dependent on gas and chamber characteristics.

One of the main activities of my experiment was to perform a *scan HV* on individual RPCs. For each detector, I measured the current as the applied voltage changed, using MobaXterm to remotely connect to the test tower computer. The procedure involved increasing the voltage from 1000 V to 9000 V, in steps of 1000 V, and then from 9000 V to 9400 V, in smaller steps of 100 V, in order to observe the detector's response in the region of interest more precisely. We subsequently optimised this procedure by writing a voltage ramping programme (paragraph 3.1).
Performing periodic HV scans on the detectors is essential to monitor the proper functioning of the RPCs and ensure that they are operating under optimal conditions. Regularly checking the transition between the ohmic and multiplication regimes allows us to diagnose any anomalies, such as gas leaks, ageing chambers or problems with voltage application. Below are the graphs of the most recent HV scan on 10/09/2024:

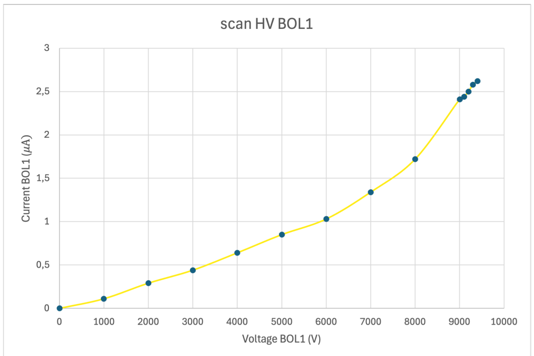

Figure 13: Scan HV BOL1

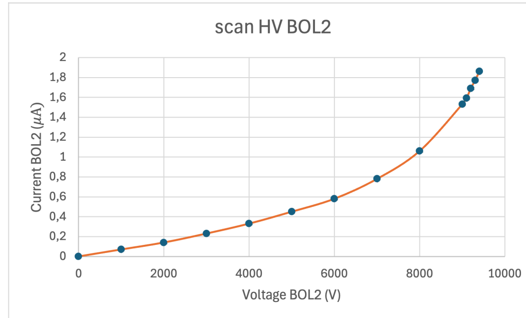

Figure 14: Scan HV BOL2

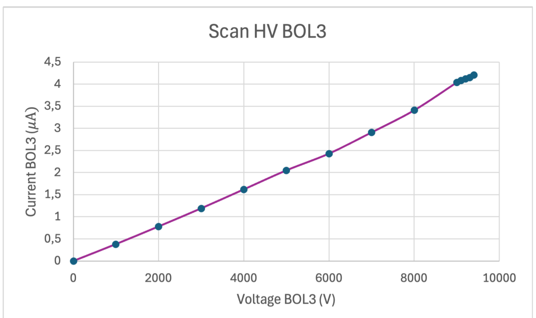

Figure 15: Scan HV BOL3

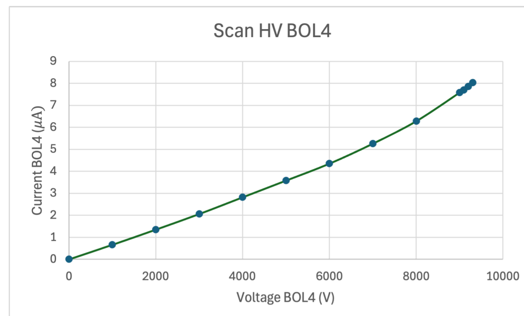

Figure 16: Scan HV BOL4

Figure 17: HV scan of the four BOLs

BOL1 BOL2: Expected behaviour

The graph of BOL1 and BOL2 follows exactly the typical behaviour of an RPC. In the initial part, at low voltages, the current increases **linearly**, indicating the **ohmic** phase, in which the gas behaves as an insulator or a weak conductor. When the voltage increases, we observe a transition to **exponential behaviour**, in which the current increases rapidly with increasing voltage. This indicates that the detector has reached the threshold of **multiplication avalanche**.

BOL3 and BOL4: Less pronounced behaviour

The graphs of BOL3 and BOL4 show similar behaviour to BOL1 and BOL2 in the linear growth phase at low voltages. However, the exponential increase in current is **less pronounced** compared to the first two detectors. Although an avalanche multiplication is observed, the effect is significantly weaker, suggesting that BOL3 and BOL4 do not perform optimally.

This could be due to various factors such as degradation or damage to the detector. This will be verified later.

4.1.1 Non-ohmic current

The second part consists of subtracting the ohmic component; one would expect the currents of the four BOLs to come remarkably close. This behaviour would suggest that the observed differences in the original currents were mainly due to variations in the ohmic component and that the non-resistive part is similar between the different configurations.
Below is the procedure for subtracting the ohmic component.

1. **Linear Fit of Current up to 5000 V**: To isolate the non-ohmic component of the current, a linear fit of the current-voltage curve (I-V) is initially performed for voltages up to 5000 V. This linear fit represents the ohmic part of the current. The equation of the linear fit is given by:

$$I_{fit}(V) = aV + b \tag{1}$$

where a and b are the fit parameters defining the slope and intercept of the line.

2. **Calculation of Ohmic Currents for Voltages from 1000 to 9400 V**: Using the parameters of the linear fit, ohmic current values are calculated for a wider range of voltages (1000 V to 9400 V). This step results in a prediction of the current that should be exclusively ohmic according to the linear model.

3. **Subtraction of Ohmic Current from Initial Values**: To isolate the non-ohmic component, the calculated values of the ohmic current are subtracted from the measured values of the total current. The resulting formula is:

$$I_{non-ohmic}(V) = I_{measured}(V) - I_{fit}(V) \tag{2}$$

This step removes the ohmic component from the total current, allowing only the non-ohmic part to be analysed.

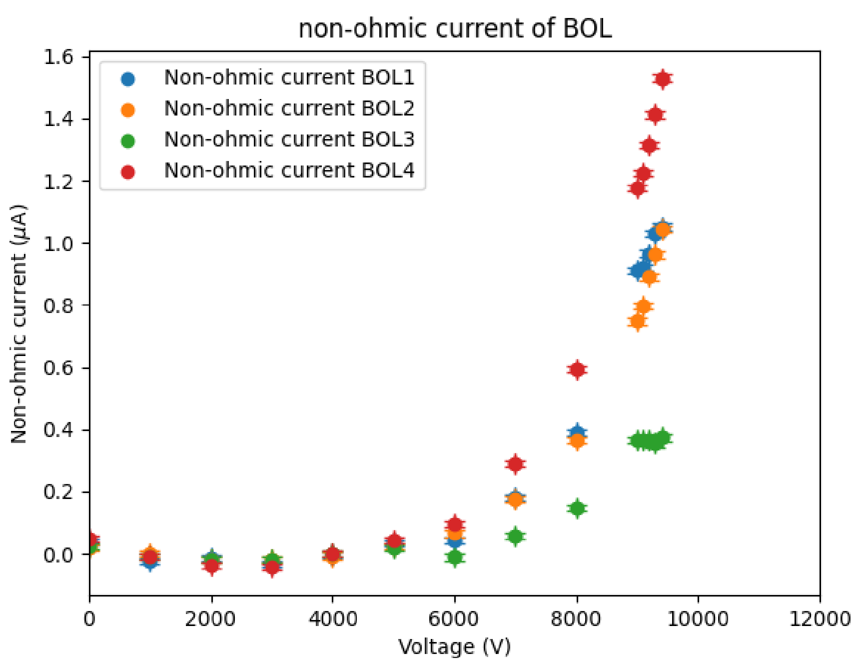

Figure 18: Comparison of the non-ohmic part of the currents flowing in the four BOLs

The graph shows the non-ohmic current measured on four different BOLs as a function of voltage. The main analysis points are shown below:

- **Rapid rise above 6000 V**: All four BOLs show a significant rise in non-ohmic current above 6000 V. This exponential trend suggests that non-linear phenomena associated with the non-ohmic component occur in this voltage region.

- **Similarities between BOL1, BOL2 and BOL3 between 6000 V and 9000 V**: In this voltage range, the non-ohmic currents of the three BOLs are very similar, confirming the hypothesis that, after removal of the ohmic component, the differences between the currents decrease significantly.
- **Deviation of BOL4 after 9000 V**: Unlike the other BOLs, BOL4 shows a much more pronounced increase in non-ohmic current above 9000 V. This behaviour might suggest the presence of other factors influencing the non-resistive behaviour for this specific BOL.

The procedure suggested that, by subtracting the ohmic component, the differences between the currents in the various BOLs should decrease. This prediction is confirmed up to about 9000 V, beyond which BOL4 exhibits divergent behaviour. This implies that while the ohmic component was predominant in the initially observed differences, BOL4 is influenced by additional non-resistive factors.

Possible explanations for the behaviour of BOL4 are:

- **Structural effects**: It is possible that physical or structural differences in the BOL4 contribute to the increase in non-ohmic current at high voltages.
- **Saturation or breakdown effects**: The sudden increase of non-ohmic current in BOL4 may indicate the onset of saturation or breakdown (dielectric discharge) phenomena, which typically occur at high voltages.

4.1.2 Effective voltage and current

In scientific experiments and technological applications, the voltage and current applied to a system can vary depending on environmental conditions, such as temperature and pressure. To obtain accurate measurements, it is essential to correct for these variables. The formula used to calculate the effective voltage (HV_{eff}) is:

$$HV_{eff} = \frac{V_{0\_set} \cdot (T + 273)}{293} \cdot \frac{1010}{P} \tag{3}$$

dove:

- V_{0_set} is the voltage set to the system (nominal voltage).
- T is the ambient temperature in degrees Celsius.
- 273 is the conversion from Celsius to Kelvin.
- 293 is the reference temperature in Kelvin (20°C + 273).
- 1010 is the reference pressure in millibars (approx. 1 atmosphere).
- P is the ambient pressure in millibars.

This formula allows a voltage value to be obtained that represents the actual voltage applied to the system under non-standard ambient conditions. Corrections for temperature and pressure are essential to ensure measurement accuracy and consistency between different environmental conditions.

To obtain the rms current (I_{eff}), we used the previously calculated non-ohmic current and calculated it using the voltage with temperature and pressure corrections. The formula used is:

$$I_{eff} = I_{mon} - (m_{retta} \cdot HV_{eff} + q_{retta}) \tag{4}$$

dove:

- I_{mon} is the measured current.

- m_{retta} is the angular coefficient of the linear fit of current against voltage, obtained for voltages up to 5000 V.

- q_{retta} is the intercept of the linear fit line.

- HV_{eff} is the rms voltage corrected for changes in temperature and pressure.

The pressure and temperature at the time of the last HV scan is:

- P = 1012,0 ± 0,1 hPa

- T = 23 ± 1 °C

The graphs obtained are as follows:

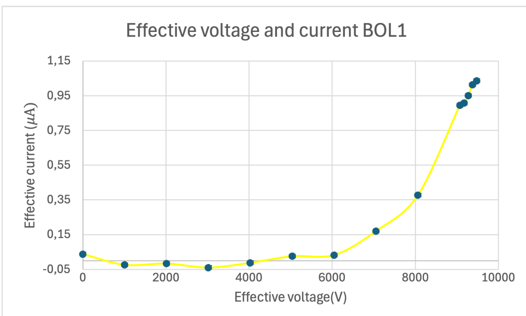

Figure 19: Effective voltage and current BOL1

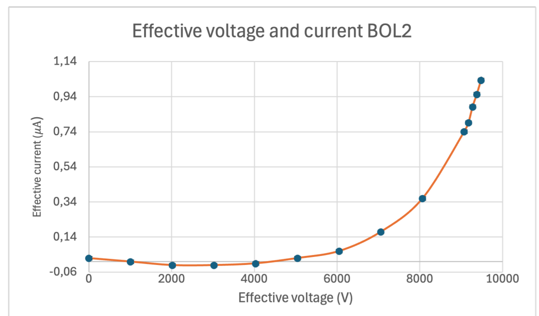

Figure 20: Effective voltage and current BOL2

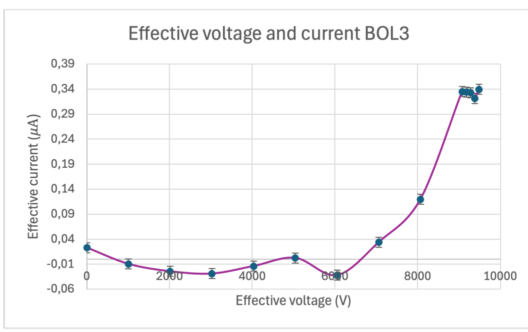

Figure 21: Effective voltage and current BOL3

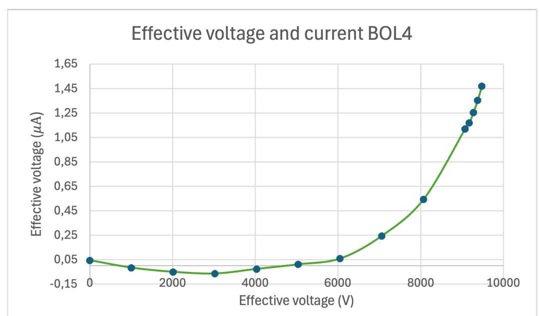

Figure 22: Effective voltage and current BOL4

Figure 23: Effective voltage and current of the four BOLs

The graph shows the relationship between the rms voltage HV_{eff} and the rms current I_{eff} for the BOL system. In general, we expect the trend of the rms current to increase with increasing rms voltage, and this is confirmed in the upper part of the graph, where a clear exponential increase is observed. However, in the lower part (up to about 6000 V), the behaviour of the current appears distorted: negative or near-zero current values are observed.

Negative currents can be caused mainly by:

- A linear fit that does not represent the low-voltage part well.

- Errors in temperature and pressure corrections.

- Instrumental noise emerging when currents are very small.

4.2 Data acquisition and analysis

During this experiment, several data acquisitions were carried out on different time intervals, before doing so it is necessary to construct the efficiency curve. Recording the efficiency curve is essential to determine the optimal working point of the RPCs, which is necessary to ensure that during data acquisitions the detector operates with maximum stability and efficiency

4.2.1 Efficiency curve of an RPC

The efficiency curve of a resistive plate chamber (RPC) detector is an important parameter in evaluating the performance of the detector. It shows the variation in detection efficiency as a function of the voltage applied to the RPC plates and typically consists of three main regions:

1. **Low efficiency region**: At relatively low voltages, the electric field generated is not sufficient to trigger the ionisation and charge multiplication process within the chambers. At this stage, the efficiency of the detector remains very low and almost constant.

2. **Rapid Efficiency Growth Region**: Above a certain voltage threshold, the efficiency of the detector increases rapidly. In this region, the electric field is strong enough to multiply the charges produced by the ionising particles, improving the detection capability.

3. **Plateau**: At even higher voltages, the detector efficiency reaches a maximum and stabilises. In this range, the RPC operates at optimum conditions, with an efficiency close to 100 per cent.

To obtain the presented efficiency curve, we used an experimental setup based on three RPC chambers, excluding the fourth chamber from the system. The electrical signal generated by the passage of charged particles through the chambers was processed as follows:

1. **Discriminators**: The electrical signal produced by the RPC chambers was sent to electronic discriminators, the purpose of which is to select only signals with an amplitude above a predetermined threshold. This step reduces background noise and ensures that only relevant signals are considered for analysis.

2. **NIM modules for coincidences**: Discriminated signals were sent to NIM modules to construct coincidences. Two types of coincidences were used:

   - **Double coincidence**: between the signals from chambers RPC1 and RPC3. This measurement allows us to verify the passage of particles through RPC1 and RPC3, regardless of the behaviour of RPC2.
   - **Triple coincidence**: between the signals of the chambers RPC1, RPC2 and RPC3. This allows us to assess the contribution of RPC2 in particle detection.

3. **Scaler**: The signals of double and triple coincidences were sent to a scaler, a device that counts the number of pulses received in a defined time interval. The scaler provides an accurate count of the coincidences, allowing the construction of the efficiency curve.

To obtain the efficiency curve, we only varied the voltage applied to RPC2, keeping the voltage on RPC1 and RPC3 constant. This choice allows us to isolate the contribution of RPC2, evaluating the efficiency of this chamber by comparing the number of triple versus double coincidences. While the double coincidence remains constant (indicating the passage of particles through RPC1 and RPC3), the number of triple coincidences increases as the voltage applied to RPC2 increases, until it reaches a plateau. During the experiment, the count of single signals from RPC1 and RPC3 was also monitored, which remained constant throughout the voltage variation range, confirming the stability of these chambers.

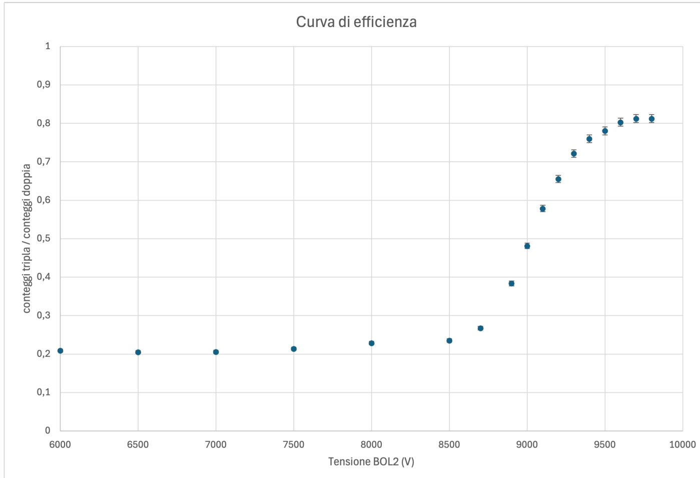

Figure 24: Efficiency curve

The efficiency curve obtained is shown in Figure ??. As expected, it presents the three trends described above:

- **Low-efficiency region**: Between 6000 V and 8500 V, the efficiency remains low (around 20%) and constant, indicating that the voltage is still not sufficient to ensure effective detection.
- **Fast growth**: Starting at 8500 V, the efficiency increases rapidly, signalling the start of proper operation of RPC2. The voltage is now high enough to activate the charge multiplication process.
- **Plateau**: After 9400 V, the curve stabilises with a maximum efficiency close to 90 per cent. This plateau represents the optimal operating region of the RPC2 chamber.

The optimum operating point for RPC2 is around 9400 V, where the detector operates efficiently and stably, with no further significant improvement as the voltage increases. The anomaly we observe is that the efficiency should be close to zero before reaching the threshold voltage; however, we notice a bottom with an efficiency of 20%, probably due to noise.
For this reason, we chose to set the acquisition voltage at 9400 V, as it represents the optimal operating point that guarantees good detector operating efficiency while maintaining stability and reliability during data collection.

Data Analysis

During this experiment, several data acquisitions were carried out on different time intervals, which can be viewed in the table (table ??). The acquisition used to generate the graphs presented below was carried out on 10 September 2024.

Acquisition Date	Number of events	BOL switched on	Type of trigger
12/07/2024 14:25:30	390000	4 BOLs switched on at 9400 V	NIM
12/07/2024 14:58:23	40000	4 BOLs switched on at 9400 V	NIM
12/07/2024 12:55:23	990000	4 BOLs switched on at 9400 V	NIM
05/08/2024 18:54:28	30000	4 BOLs switched on at 9400 V	FPGA
10/09/2024 13:07:17	500000	4 BOLs switched on at 9400 V	NIM

Figure 25: Acquisition table

The raw data must be converted into a rootpla format using a dedicated executable. Next, we use a Python programme to convert this data into events, using the HitToEvent software.

In an apparatus consisting of four RPCs (Resistive Plate Chambers), an event is the interaction of a particle with the entire detection system. As the particle passes through the system, information is collected on two fundamental coordinates: the azimuthal coordinate ϕ and the pseudorapidity coordinate η.

A hit represents a single signal recorded on one of the two coordinates (ϕ or η) in an RPC layer. Since each RPC records both the ϕ and η co-ordinates, a complete crossing of a particle in an RPC should ideally produce two hits (one for ϕ and one for η).

Since the apparatus consists of 4 RPCs, under ideal conditions we expect 8 hits for each event, i.e. 4 layers, each with two hits for ϕ and η). However, our analysis focuses on 3 RPCs and the selection of golden events, so the ideal number of hits is 6. Let us see in detail what the golden events are: The data analysis focuses on the analysis of three RPCs and focused on *Golden* events. We define *Golden* events as those events that hit the three RPC detectors twice, once for each η and ϕ coordinate. We thus obtain a total of 6 co-ordinates which together form a good trigger. We obtained these results using a program written in `PyROOT` language, imposing specific conditions to isolate these types of events. An important aspect to evaluate in this experiment is the percentage of "golden" events, i.e. those events that meet certain selection criteria. The calculation of this percentage is simple and is based on the ratio between the number of "golden" events and the total number of events recorded. The formula for the percentage is as follows:

$$\%_{golden} = \left(\frac{N_{golden}}{N_{total}} \right) \cdot 100 \tag{5}$$

dove:

- $N_{golden} = 52694$ is the number of 'golden' events.
- $N_{totali} = 499996$ is the total number of recorded events.

Substituting the values into the formula we obtain:

$$\%_{golden} = \left(\frac{52694}{499996} \right) \cdot 100 \approx 10.54\% \tag{6}$$

Unfortunately, as can be seen, the percentage of 'golden' events is only about 10.54%. This value is rather low, suggesting that a large proportion of the events do not meet the required criteria.
On a positive note, as can be seen from the HV scans (section 4.1), the BOL4, albeit not very pronounced, shows the required trend. Furthermore, as can be seen from the hit channels, several hits were recorded in BOL4. Consequently, I proceeded to calculate its efficiency.

The efficiency is given by the ratio between the number of hits (the hit may be on either the /*eta*-coordinate or the *phi*-coordinate or either one) recorded in the BOL4 and the total number of golden events. The formula used is as follows:

$$\text{Efficiency} = \frac{\text{Number of BOL4 hits}}{\text{Total number of golden events}}$$

Entering data:

$$[\text{Efficiency} = \frac{20918}{52694} \approx 0.397$$

Thus, the efficiency of the BOL4 is approximately 39.7%.

Although the calculated efficiency value is positive, it must be considered that this is a relatively small number, as we are considering that even only one of the η and ϕ channels is contributing to the hit count. Furthermore, as BOL4 is the last RPC chamber, many of the high-angle tracks are lost, further reducing the number of hits recorded.

This result suggests that the detector needs fine-tuning. However, we remain confident because, looking at the displays showing individual events, we notice that we can identify straight tracks so the detector is able to function as a trigger.

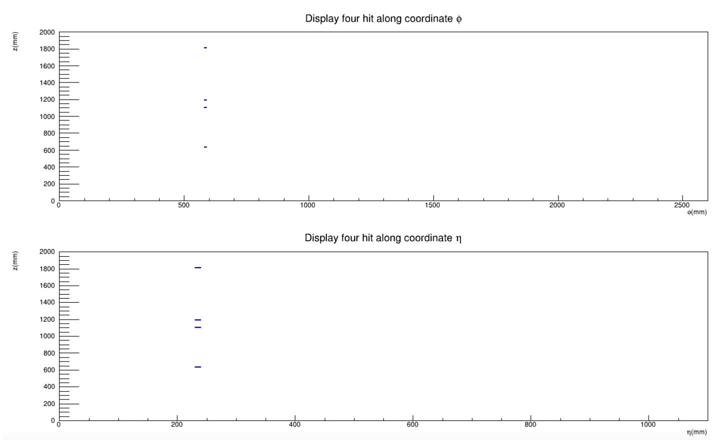

Figure 26: event-by-event display

4.2.2 Distribution of hits along TDC channels

An important graph to be realised is the distribution of the *hits* as a function of the TDC (Time-to-Digital Converter) channel. The mapping of the TDC channels is as follows:

- Channels 0 to 13 are associated with RPC 1.
- Channel 15 is the FPGA trigger.
- Channels 16 to 29 are associated with RPC 2.
- Channels 32 to 45 are associated with RPC 3.
- Channels 48 to 61 are associated with RPC 4.

In particular, the first four channels are associated with the *eta* co-ordinate and require specific evaluation. This subdivision allows us to analyse the response of each RPC with respect to specific TDC channels, highlighting the distribution of *hit* according to the channel.

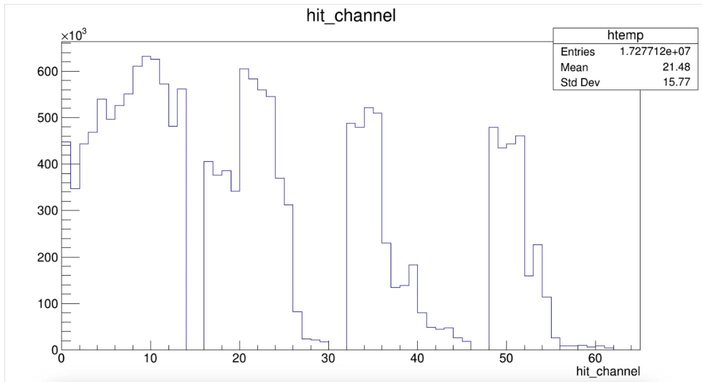

Figure 27: hit channel distribution

In the case of RPC 1, we observe that all the channels are overly active, suggesting that it is likely affected by significant noise

The behaviour observed in RPC 3 is similar: the final *phi* channels (41 to 45) show an irregular distribution with a very low number of hits. Also in this case, the channels appear not to register events correctly.

In contrast to the other detectors, RPC 4 also shows an even distribution of hits in the final *phi* channels. This suggests that the problem observed in the end channels of RPC 1, 2 and 3 may not be systematic, but specific to those detectors.

With regard to the first 4 channels, associated with the ϕ coordinate, we can observe a more regular distribution of hits than in the final ϕ channels.

Further investigation is needed, both at hardware (connections, electronics) and software level (calibration, data processing), to determine the cause of the behaviour observed in the final ϕ channels.

4.2.3 Distribution of hits

I made graphs of the distribution of total hits and golden events for the entire data set.

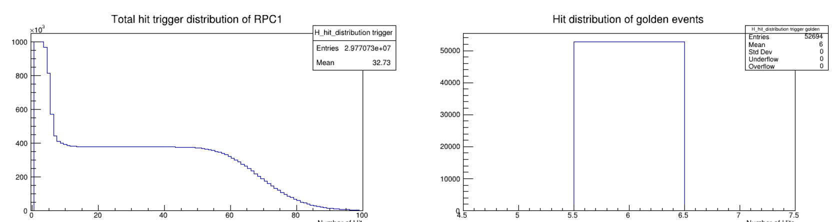

Figure 28: Left: the distribution of total hits; right: the distribution of golden event hits

The graph on the left shows the distribution of the total number of hits recorded for each event.Ideally, each event should generate 8 hits, as each RPC records both ϕ and η coordinates.

We observe that the main peak is around 10 hits, and the graph rapidly decreases for higher hit values. This means that although noise is present in the system (with more hits than expected), it is not excessive. The fact that most events present 10 hits, close to the ideal value of 8, indicates that the noise is under control.

The graph on the right shows the distribution of hits in so-called golden events, i.e. high-quality events in which every particle crossing is correctly recorded without significant interference or distortion. As we expect, the distribution peaks at exactly 6 hits, which is the ideal number for a ‘perfect’ event in which every particle correctly crosses the system recording both the ϕ and η coordinates in each RPC.

This result confirms that, at least for golden events, the system operates exactly as expected, recording the correct number of hits. However, despite this ideal behaviour, it is important to note that the percentage of golden events in relation to the total number of events is still low, suggesting that noise could compromise a significant part of the collected data.

Distribution of hits along the ϕ coordinate

Cosmic rays arrive at the Earth's surface from all directions. However, their distribution is nearly isotropic, i.e. they come from all directions with equal probability, if measured in a sufficiently large spatial volume and in an environment unaffected by atmospheric or geomagnetic effects, one would expect a 'domed' distribution of hits, this because muons, which are the main product of the interaction of cosmic rays with the atmosphere, impact on the detector area with a certain homogeneity. This should generate a central peak hit, with a gradual decrease as one moves away from the centre of the detector. Under ideal conditions, one would expect such a distribution for each RPC: a central peak due to the geometry of the detector and the trajectory of the cosmic rays through the apparatus. By observing the graphs of the distribution of hits along the front ends for each RPC and comparing the results with expectations, we can make some important observations.

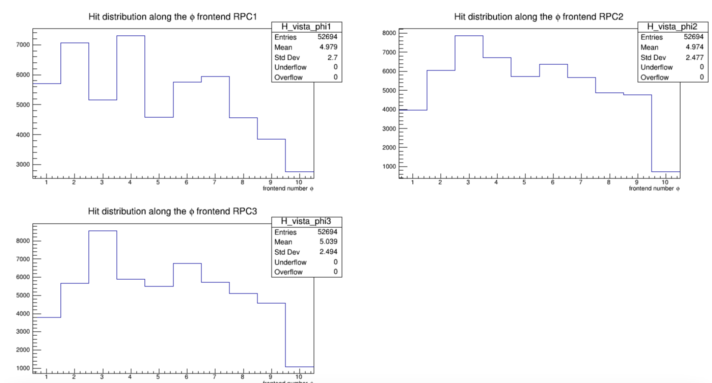

Figure 29: Distribution of hits along the ϕ coordinate.

In the graphs of the distribution of hits along the frontends, we observe a rather irregular distribution, with some unexpected peaks and a lack of the symmetry typical of a 'dome' distribution. Only one of the RPCs shows a vague resemblance to the expected distribution. In addition, we note that the right-hand side of the graph shows a lower number of hits; already from the hit channel graph we observed less activity in this region.

- **Statistics limited**: Golden events, being less frequent, may not generate enough data to form a uniform and symmetrical distribution. The scarcity of events may lead to random fluctuations in the counts for each frontend ϕ, causing an uneven distribution.
- **Geometrical effects**: Not all detectors may have an ideal geometry or there may be inefficiencies in the detection of hits on certain front ends. This could explain the absence of a regular dome shape.
- **Detector efficiency**: Some RPCs might have a better detection efficiency than others, contributing to irregular peaks in the distribution of hits. The right-hand side of the graph, in particular, was expected to be less represented, as confirmed by observing the hit channel graph, where reduced activity in that area was already noticeable.

4.2.4 Time of Flight

One of the most relevant graphs I made was the one representing the time of flight (*Time of Flight*, TOF) between pairs of RPCs, i.e. between RPC1 and RPC2 and RPC1 and RPC3. I have not calculated the time of flight between RPC2 and RPC3 because the distance between them is so small, about 40 cm, that the resulting time of flight would be less than the available temporal resolution. In order to calculate the time of flight, I recorded the time at which each RPC's η and ϕ coordinates record the *hit*. Subsequently, I filled the TOF histogram between the pairs of RPCs with the recorded time differences between the *hit* of each pair.

Importance of time-of-flight calculation Since we are detecting muons, it is essential that the results are compatible with physics. Muons, being relativistic particles, travel at speeds very close to that of light. Knowing the distance between the detectors, we expect a time of flight compatible with the speed of light (c).

The distances, approximating them to straight tracks, are as follows:

- RPC1 is located at 1815 mm,
- RPC2 is located at 1190 mm,
- RPC3 is located at 1100 mm.

The time of flight t_{TOF} can be calculated as:

$$t_{TOF} = \frac{d}{c}$$

where d is the distance between two RPCs and c is the speed of light, which is approximately 299.792 mm/ns.

Calculating the expected flight times:

- Between RPC1 and RPC2: $t_{TOF} \approx 2084\,\text{ps}$,
- Between RPC1 and RPC3: $t_{TOF} \approx 2385\,\text{ps}$.

These values represent the expected time interval for the muons to pass between the RPC pairs, and a comparison with the experimental data allows us to verify compatibility with theoretical expectations and thus the correct interpretation of the data.

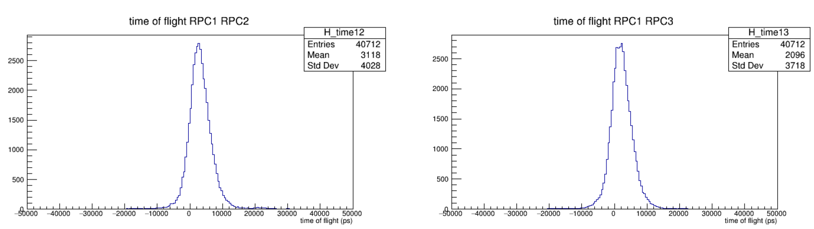

Figure 30: Time of flight

From the graphs provided for the η and ϕ coordinates, we can make some observations comparing the experimental results with the theoretical expected flight times.

Expected theoretical flight times

a) RPC1 - RPC2

- **Average TOF**: 3113 ps
- **Standard deviation**: 4028 ps

The measured mean of 1996 3718ps is significantly higher than the expected value of 2385 ps. The very large standard deviation suggests that the data is very scattered, with a possible presence of noise or inefficiencies in the detectors. furthermore, I made an approximation by considering only straight tracks.

b) RPC1 - RPC3

- **Average TOF**: 1926 ps
- **Standard deviation**: 3797 ps

The average of 1926 ps is lower than the expected value of 2385 ns, but is within a reasonable margin, considering the large dispersion of the data and the fact that I made an approximation by considering only straight tracks. Again, the large standard deviation suggests considerable variability in the times recorded.

The experimental results show discrepancies from the theoretical flight times expected for relativistic muons. The presence of high standard deviations and negative values suggests the need for further investigation of the calibration and timing mechanisms of the RPC detectors. A review of the efficiency of the detectors and possible sources of noise will be necessary to improve the accuracy and reliability of the measurements.

One of the factors that could explain the abnormal flight times is the delay introduced by the distance between the recording channel and the electronic front-end. In other words, if the signal has to travel a greater distance within the acquisition system, it could be recorded with a delay compared to other signals.

Procedure:

1. **Straight Track Selection**: This selection allows the effects of curved tracks to be minimised.
2. **Focus on channel** $\eta 4$: This channel shows the greatest time dispersion in the calculations I performed.
3. **Creation of a histogram**: The histogram will show the average values and respective errors of the trigger time recorded on $eta4$, as a function of the position of a given channel ϕ.

The objective is to calculate a correction for the signal recording time so that the theoretical values of the flight time correspond to the measured values.

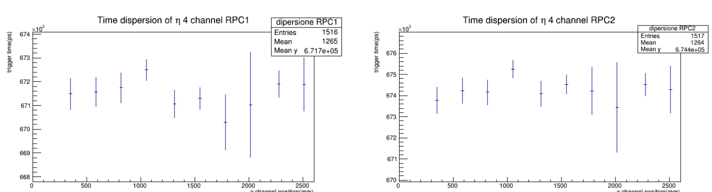

Figure 31: Time distribution of channel $\eta 4$ as a function of channel ϕ position.

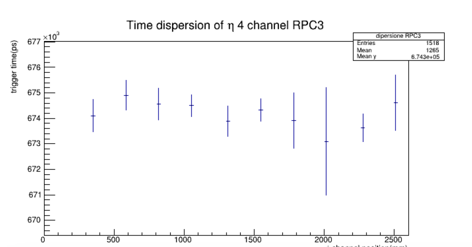

Figure 32: Time distribution of channel $\eta 4$ as a function of the position of channel ϕ.

It is observed that the time dispersion along channel $\eta 4$ with respect to the ϕ coordinate is not as expected. As far as RPC1 and RPC2 are concerned, the first four channels show an increasing trend, suggesting that more time is taken to trigger for channels with higher ϕ values. However, this trend is not repeated for the final part of the ϕ channel, where problems had already been found by observing the distribution of hits. In particular, the last ϕ channels are less irradiated.

4.2.5 Distribution of parameter β

Looking at the distribution of the parameter β, defined as the ratio of the Euclidean distance between two RPCs divided by the time of flight normalised to the speed of light, we would expect this value to be very close to 1. However, we observe similar anomalies to those seen in the analysis of the time of flight.

For the calculation of β, we use the following formula:

$$\beta = \frac{d}{t \cdot c}$$

where:

- d is the Euclidean distance between two RPCs,
- t is the measured time of flight,
- c is the speed of light in vacuum.

In particular, for β between RPC1 and RPC3, we note that the average is rather high, peaking at around 0.6, which represents a value below the speed of light ($\beta < 1$). This behaviour is not expected, since β should be much closer to 1 for relativistic particles.

Furthermore, we observe some values of $\beta > 1$, which indicate anomalous flight times, suggesting measurement errors or delays in signal acquisition. To correct these anomalies, we can apply a physical cut on the data, removing measurements with $\beta > 1$ that have no physical significance for subluminal particles.

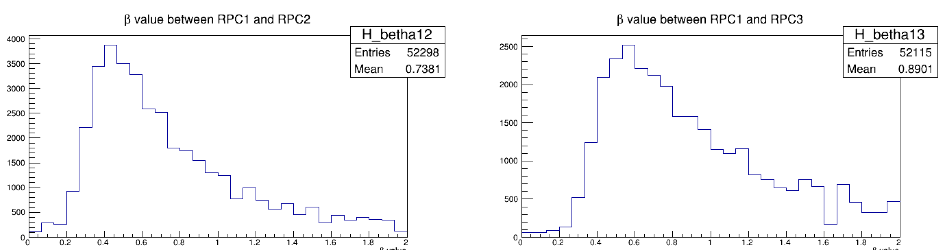

Figure 33: Distribution of β between RPC1 and RPC2 (left) and between RPC1 and RPC3 (right).

5 Conclusions

During this experience, I carried out a series of RPC detector tests using a test tower consisting of four BOL detectors, similar to those present in the ATLAS experiment. In particular, I was responsible for the assembly of the chambers, the handling of the high voltage (HV) and the data acquisition system (TDAQ), with the aim of verifying the correct functioning of the detectors and optimising their performance.

Through the HV scans and the analysis of the efficiency curve, I was able to observe that the BOL1 and BOL2 detectors behaved as expected, with a clear transition from the ohmic phase to the avalanche multiplication phase. In contrast, BOL3 and BOL4 exhibited less pronounced behaviour, suggesting possible inefficiencies that may require further calibration. The analysis of the 'golden' events also confirmed the detectors' ability to act as triggers, although with a percentage that can still be improved.

In summary, I can conclude that the tower is ready to accommodate the new BI chambers. However, a fine-tuning of the BOL4 chamber is necessary to optimise its operation and ensure the overall operational efficiency of the system.